

Automated active learning in seismic image interpretation

Haibin Di¹ and Aria Abubakar¹

<https://doi.org/10.1190/tle41090628.1>

Abstract

Three-dimensional seismic interpretation has been significantly accelerated by the recent implementation of various machine learning algorithms, particularly supervised convolutional neural networks (CNNs). CNNs are able to parse seismic data from the perspective of pattern recognition, extract seismic features at multiple scales, and provide acceptable predictions. The performance of a supervised CNN in seismic image interpretation greatly depends on its training labels, which are usually a set of seismic sections with expert annotations. Among the thousands of sections in a typical 3D seismic cube, effectively selecting those that are most representative is a challenging task. A common approach is to have an experienced interpreter visually screen all of the sections and make their selection. To improve the efficiency of training section selection and to avoid introducing bias from manual screening, this work proposes an automated-active-learning (AutoAL) workflow for interactive seismic image interpretation. This enables quantitatively evaluating the machine performance after one iteration and efficiently recommending the sections to be labeled for learning in the next iteration. The added value of the proposed approach is validated through an application of seismic facies classification to the Parihaka data set in the northwest part of offshore Taranaki Basin in New Zealand. Starting from four initial sections, in three iterations the proposed AutoAL automatically recommends 14 from more than 1300 sections as training data. This improves the accuracy and average F1 of the machine prediction over 0.9. Comparisons demonstrate better prediction by the proposed scheme over traditional training section selection schemes, such as manual screening and clustering-based recommendation.

Introduction

Seismic data play an essential role in delineating geologic structures and estimating rock properties in the subsurface. Thus, seismic data have wide application in near-surface mapping, reservoir characterization, CO₂ storage monitoring, etc. Given its importance, computer-aided seismic interpretation has been a research focus for decades. It produces a set of automated tools for greatly accelerating the process of seismic interpretation including 3D visualization, horizon tracking, fault picking, attribute analysis, structural modeling, property estimation, etc. Take attribute analysis for example. Structures over the seismic resolution are detectable as distorted patterns in a seismic image. They can be lineament shaped for faults, dome shaped for salt bodies, meandering for channels, and chaotic cone shaped for gas chimneys. Therefore, an efficient seismic attribute can be defined as a math operator that is capable of optimally quantifying such distortions. Some of the most popular attributes include instantaneous

phase/frequency (Taner et al., 1979; Robertson and Fisher, 1988; Barnes, 2007), coherence (Bahorich and Farmer, 1995), semblance (Marfurt et al., 1998), dip (Marfurt and Kirlin, 2000), curvature (Roberts, 2001), gray-level co-occurrence matrix-based texture (Gao, 2003), similarity (Tingdahl and de Rooij, 2005), fault likelihood (Hale, 2013), salt likelihood (Wu, 2016), flexure (Di and Gao, 2017), etc. Multiattribute analysis becomes feasible with the aid of red-green-blue rendering and simple machine learning algorithms such as self-organizing mapping (Roy et al., 2010), *k*-means clustering (Di et al., 2018a), artificial neural networks (Zheng et al., 2014), and convolutional neural networks (CNNs) (Huang et al., 2017). These further improve the interpretation experience compared to using a single attribute.

Meanwhile, the recent emergence of deep learning, especially CNNs, makes it possible to interpret a seismic volume from its amplitude without involving typical deterministic seismic attributes. Some of the most successful applications are fault detection (Di et al., 2018b; Guittot, 2018; Xiong et al., 2018; Wu et al., 2019a), salt-body delineation (Waldehand et al., 2018; Shi et al., 2019; Di and AlRegib, 2020), horizon tracking (Peters et al., 2019; Wu et al., 2019b; Tschanne et al., 2020), sequence analysis (Li et al., 2019; Di et al., 2020), and integrated interpretation (Di et al., 2019; Guo et al., 2020). Most of these CNN applications in seismic interpretation are supervised learning. This requires an interpreter to annotate a set of seismic sections as training data. However, manual efforts are limited, and correspondingly, the annotated training sections are only a small part of an entire seismic volume and fail to represent the complexities in seismic patterns well within the seismic survey. In such a case, although a CNN effectively learns from the annotated sections, its generalization capability is limited, causing its prediction on the sections far away from the training ones to be least acceptable. To improve machine performance, a common strategy is to (1) expand the training data by sorting and annotating the challenging sections, (2) retrain and evaluate the CNN, and (3) repeat the process until the machine prediction becomes acceptable. For such iterative seismic interpretation, active learning (AL) (Das et al., 2016) appears to be a good fit, in which a CNN can interactively query an expert to annotate new seismic sections where its prediction is least accurate. However, without a volumetric annotation for quantitative analysis, such section-wise evaluation of CNN prediction still greatly depends on visual screening based on an interpreter's knowledge. This is labor intensive and subjective.

In this paper, we propose a new seismic image interpretation workflow powered by automatic AL (AutoAL). This not only enables the desired interactive process of an interpreter providing feedback from one iteration to the next but also implements a relative geologic time (RGT) reconstruction error (RRE)-based

¹Schlumberger, Houston, Texas, USA. E-mail: hdi@slb.com; aabubakar@slb.com.

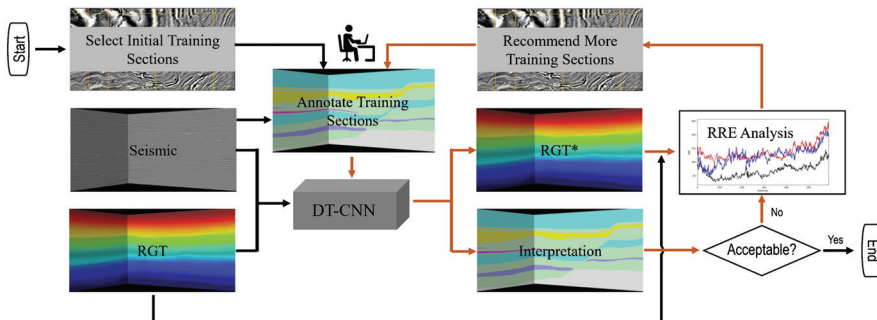


Figure 1. The proposed AutoAL workflow for interactive seismic image interpretation that implements a dual-task seismic interpretation CNN and enables automated training section recommendation based on RGT-RRE analysis.

scheme capable of automatically evaluating the machine prediction and recommending the training sections necessary for the next iteration. An example of seismic facies identification is used to demonstrate the added value of the proposed AutoAL-powered seismic image interpretation. It also demonstrates the improved performance of the RRE-based scheme over other schemes in selecting the most representative training sections from thousands of seismic sections for optimal CNN learning.

Workflow description

Figure 1 illustrates the proposed AutoAL workflow for interactive seismic image interpretation. The workflow consists of the following four components.

Data preparation. In addition to seismic amplitude, the workflow requires a few sections for initializing the iterative process. These sections can be selected by manual screening or clustering-based recommendation (Manikani et al., 2022) and annotated according to the interpretation objective such as facies classification. The addition is RGT, which is involved in multiple pieces of the proposed workflow including training the dual-task CNN (DT-CNN), quantifying the prediction errors, and recommending sections for the next iteration of CNN training. Among various RGT schemes, we use the FlowNet-based algorithm to generate the RGT volumes used in the later examples. The algorithm first uses the seismic FlowNet (Li and Abubakar, 2020) to estimate the relative displacements (or flow vectors) between adjacent seismic sections. It then constructs the corresponding RGT by extracting a dense set of horizons based on the estimated flow vectors.

Label annotation. Another essential component is an interpreter's involvement in formulating their interpretational objective of the target seismic data set as annotations that can be digitalized and used for training the DT-CNN. For both the initial and recommended sections, the manual annotation is expected to be comprehensive for every section and consistent across sections. Uncertain zones are required to be marked so they can be excluded from learning.

DT-CNN. As the core of the proposed workflow, the next step is to train a DT-CNN with its architecture (Figure 2), which uses seismic and RGT as the input features and expert annotations as the learning target. Specifically, the DT-CNN starts with a pretrained feature engine that learns from the input seismic and

RGT. This is followed by an encoder-decoder block for multiscale feature extraction. It ends with two output branches: one to match the expert annotations and the other to reconstruct the RGT on the specified training sections. Correspondingly, the loss function \mathcal{L} is defined as

$$\mathcal{L} = \mathcal{L}_{SI} + \alpha \times \mathcal{L}_{RGT} + \beta \times \mathcal{L}_2, \quad (1)$$

where \mathcal{L}_{SI} is the cross-entropy error between the annotated and predicted seismic interpretation, \mathcal{L}_{RGT} is the mean-square-error between the input and reconstructed RGT, and \mathcal{L}_2 is the \mathcal{L}_2 regularization term. α and β are two regularization factors. Originally proposed in Di et al. (2022), such a DT-CNN demonstrates the capability of enforcing the lateral consistency preserved in RGT while building the mapping relationship between seismic and interpretation. Compared to the typical single-task CNN (i.e., U-Net), it leads to improved machine prediction, particularly when the training sections are limited in amount and/or diversity. However, the associated benefit for AutoAL was not documented in Di et al. (2022).

Applying the trained DT-CNN to the entire survey generates two results cubes. One is the predicted interpretation volume from the first output branch. The other is the reconstructed RGT volume from the second output branch. Both are of the same coverage as the input seismic survey.

Performance QC. The last component is the review and evaluation of both machine outputs. It is recommended to have the predicted interpretation volume reviewed by seismic interpreters and to quantify the corresponding prediction accuracy if certain validation sections are available. If the accuracy is acceptable, the predicted interpretation cube can be exported for future interpretation modules and tasks. Otherwise, steps 2–4 can be repeated by recommending more training sections using the automated scheme noted here, expanding the training data, enhancing the DT-CNN capability, and improving the accuracy of machine prediction.

For the reconstructed RGT (R^*) volume, its quantitative error analysis is relatively straightforward, given the input RGT (R). More specifically, for the purpose of 2D section recommendation in this paper, we propose evaluating the RGT REE along inline and crossline directions:

$$RRE_i = \sum_{j,k} \|R_{i,j,k} - R_{i,j,k}^*\|$$

and

$$RRE_j = \sum_{i,k} \|R_{i,j,k} - R_{i,j,k}^*\|, \quad (2)$$

where i , j , and k are the inline, crossline, and vertical dimensions of the seismic survey, respectively.

The motivation for using RRE for training section recommendation stems from the fact that the predicted interpretation

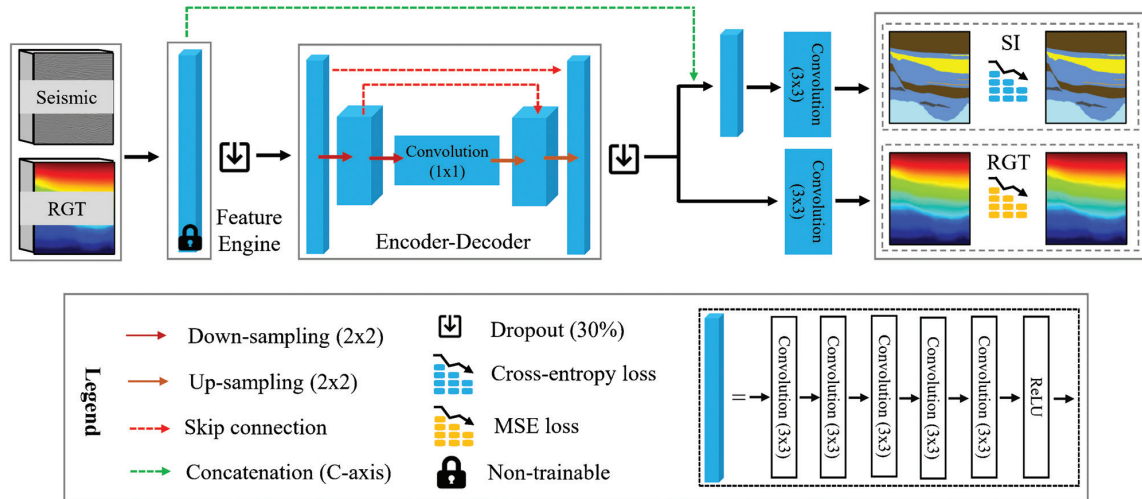


Figure 2. The architecture of the dual-task seismic interpretation CNN, which uses seismic and RGT as the input and aims at learning the expert annotations provided in the training sections and reconstructing the RGT from the same encoder-decoder block.

and reconstructed RGT originate from the same encoder-decoder block (Figure 2). Therefore, any misprediction in the predicted interpretation will be traceable in the reconstructed RGT. In other words, the larger the RRE is, the less accurate the predicted interpretation will be. Such an inverse relationship is observed when applying the DT-CNN (Figure 2) to the use case of facies classification on the Parihaka data set, in which three of the 782 crossline sections are used as training data. Figure 3 displays the corresponding RRE_i curve in red and the F1 score of predicted facies in blue. This demonstrates a Pearson correlation coefficient of -0.586. More specifically, low RRE is estimated near the three training sections. However, the error increases toward the in-between sections, while the F1 decreases from the three training sections to the rest. Similar observations are made in Figure 4. The figure shows that zones where the RGT is not well reconstructed are also those of incorrect machine prediction (denoted by circles). Therefore, in the cases of no manual annotation for machine prediction validation, it appears reasonable to use the RRE curve to (1) rapidly sort all of the sections according to their complexities for a machine to learn and capture, (2) roughly identify the sections that have been least learned by the machine, and (3) add them to the library of

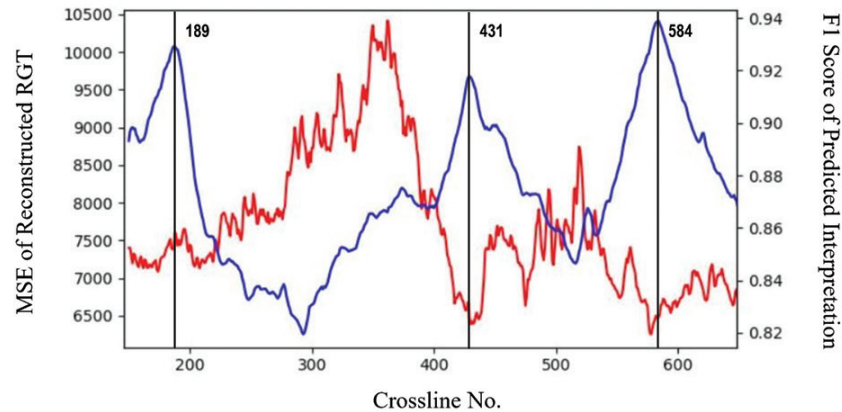


Figure 3. The inverse relationship between the RGT RRE (red) and the machine prediction F1 (blue) observed in the example of applying the DT-CNN (Figure 2) to the Parihaka data set for facies classification. The Pearson correlation coefficient between two curves is estimated to be -0.586.

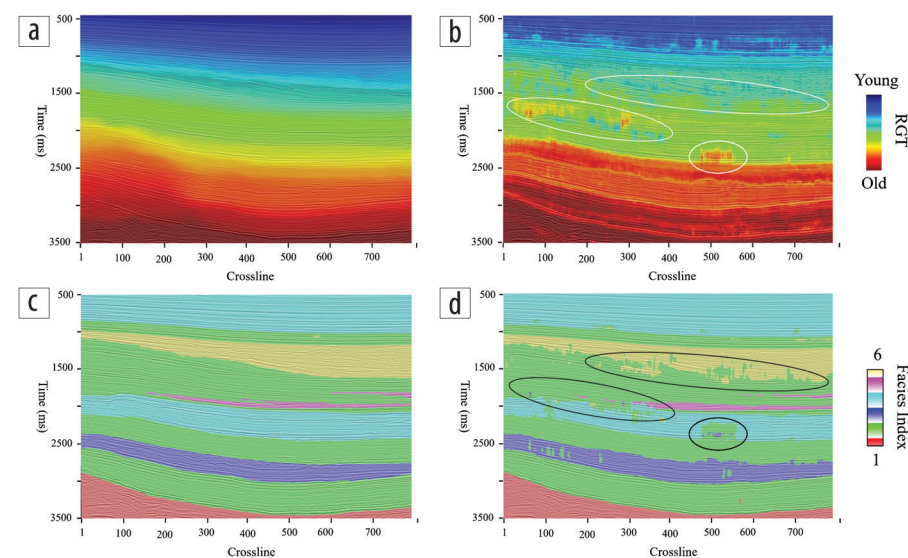


Figure 4. Visual comparison of the reconstructed RGT and the predicted facies on the Parihaka data set using the DT-CNN (Figure 2). The zones of wrong facies prediction are those where the RGT is least well reconstructed (circles), supporting the inverse relationship illustrated in Figure 3.

training data for the next iteration of DT-CNN training and prediction (steps 2 and 3).

Examples

To verify the performance of the proposed AutoAL workflow, we apply it to a subset of the Parihaka data set for facies identification. The seismic survey covers an area of approximately 150 km² in offshore Taranaki Basin, west of the North Island of New Zealand. It consists of 591 inlines, 782 crosslines, and 1006 samples per trace, with a 3 ms sampling interval (Figure 5). In addition to the seismic volume, the provided data include the corresponding RGT volume estimated by the seismic FlowNet (Li and Abubakar, 2020) (Figure 6a) and manual annotation of six facies over the entire subset. This includes (1) basement/other, (2) slope mudstone A, (3) mass transport deposit, (4) slope mudstone B, (5) slope valley, and (6) submarine canyon system (Figure 6b). Among them, facies 3, 5, and 6 are considered to

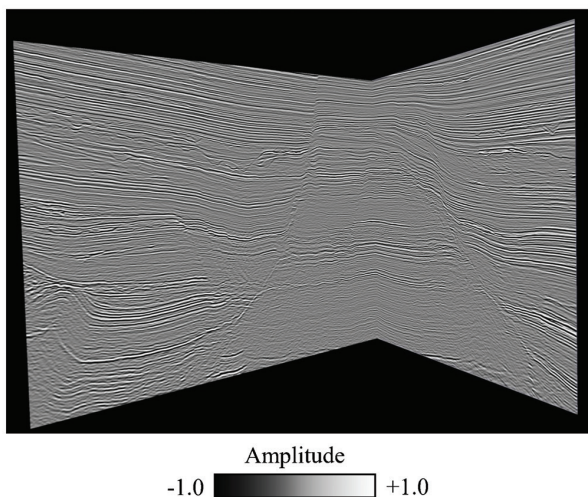


Figure 5. A 3D view of the Parihaka seismic survey used for illustrating the added value of the proposed AutoAL-enabled interactive seismic interpretation.

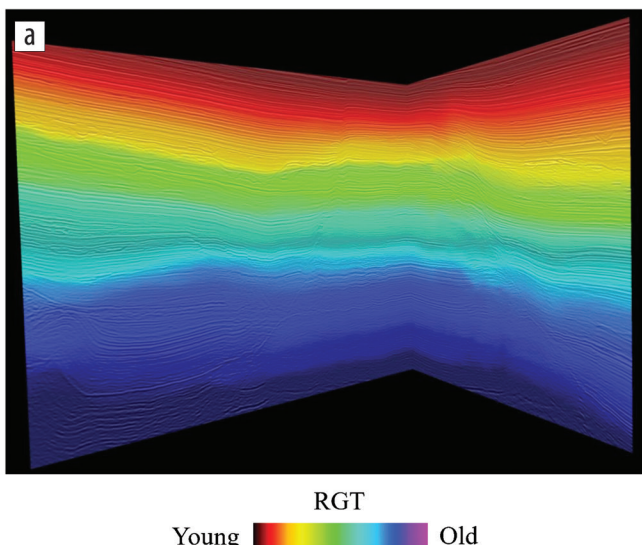


Figure 6. A 3D view of (a) the RGT volume estimated by the seismic FlowNet and (b) the manual annotation volume for evaluating the machine predictions by the proposed AutoAL workflow.

have stronger geologic implications and higher interpretational priorities. They are relatively small in amount compared to the other three facies. Correspondingly, the 20 times weight is assigned to the three facies when quantitatively evaluating the machine predictions in Tables 1 and 2.

Figures 7–9 illustrate the proposed iterative facies identification, with the training section recommendation shown in Figure 7, the RRE curves shown in Figure 8, and the 3D view of facies predictions over two validation sections (IL493 and XL143) shown in Figure 9. The process starts with four initial training sections (IL78, IL528, XL32, and XL732) that an interpreter specifies (denoted as red lines in Figure 7), from which the first iteration of DT-CNN training and prediction produces both a facies prediction cube and an RGT reconstruction cube. Comparing the latter with the input RGT cube using equation 2 derives the RRE_i and RRE_j curves (denoted as red curves in Figure 8). From the error curves, two sections (IL451 and XL431) are recommended, where the RRE reaches its local maximum (AutoAL-R1) (denoted as blue arrows in Figure 8), and added to the training data (denoted as blue lines in Figure 7). Correspondingly, a total of six sections are used for retraining the DT-CNN in the second iteration. Then, both RRE curves are recalculated and shown as the blues curves in Figure 8. Similarly, three sections (IL285, XL189, and XL584) (denoted as black lines in Figure 7 and black arrows in Figure 8) are recommended (AutoAL-R2) and added for the third iteration. Corresponding RGT errors are represented as black curves in Figure 8, from which nine sections (IL17, IL219, IL392, IL508, IL576, XL91, XL357, XL521, and XL770) (denoted as green lines in Figure 7 and green arrows in Figure 8) are recommended (AutoAL-R3). The fourth iteration of DT-CNN uses a total of 18 sections as training data. Figure 8 displays the corresponding RRE curves in green. As expected, from iteration 1 to 4, the RRE reduces significantly over all sections including the three validation sections (IL150, IL493, and XL143). Meanwhile, the facies prediction is greatly improved, as observed in 3D along validation sections IL493 and XL143 (Figure 9) and

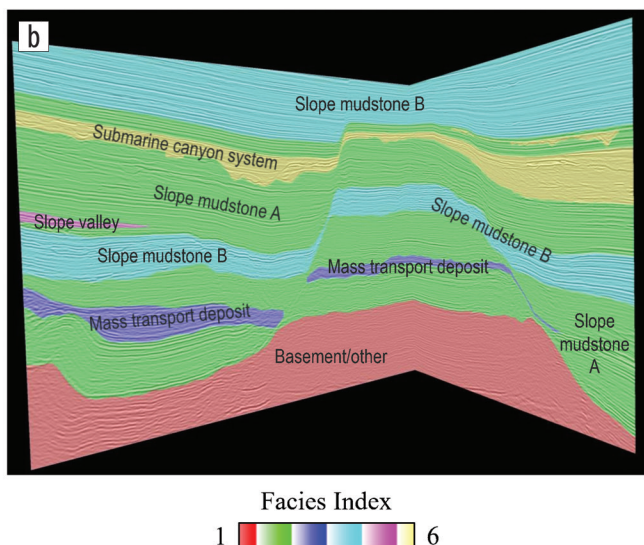


Table 1. Accuracy, precision, recall, and F1 scores of facies identification by the proposed AutoAL-enabled interactive seismic interpretation on the Parihaka data set.

Facies index	Iteration 0			Iteration 1			Iteration 2			Iteration 3		
	Precision	Recall	F1									
1	0.992	0.909	0.949	0.981	0.934	0.957	0.997	0.932	0.964	0.988	0.984	0.986
2	0.865	0.757	0.808	0.837	0.830	0.833	0.935	0.886	0.910	0.973	0.934	0.953
3	0.596	0.764	0.669	0.711	0.873	0.784	0.798	0.900	0.846	0.879	0.953	0.915
4	0.719	0.884	0.793	0.910	0.840	0.874	0.906	0.988	0.945	0.961	0.992	0.976
5	0.109	0.866	0.193	0.349	0.722	0.471	0.534	0.885	0.667	0.541	0.942	0.687
6	0.434	0.448	0.441	0.604	0.806	0.691	0.858	0.875	0.866	0.919	0.940	0.929
	Average F1: 0.642 Accuracy: 0.785 Average F1*: 0.454 Accuracy*: 0.548			Average F1: 0.768 Accuracy: 0.849 Average F1*: 0.660 Accuracy*: 0.681			Average F1: 0.866 Accuracy: 0.920 Average F1*: 0.800 Accuracy*: 0.845			Average F1: 0.908 Accuracy: 0.959 Average F1*: 0.850 Accuracy*: 0.902		

*20 times more weight on facies 3, 5, and 6 than facies 1, 2, and 4, considering their greater geologic implication and interpretational importance.

Table 2. Accuracy, precision, recall, and F1 scores of facies identification from the DT-CNN (Figure 2) trained using nine sections selected by three training section selection schemes including manual screening, clustering-based recommendation, and the proposed REE-based recommendation.

Facies index	Manual screening			Clustering-based recommendation			REE-based recommendation		
	Precision	Recall	F1	Precision	Recall	F1	Precision	Recall	F1
1	0.996	0.894	0.942	0.999	0.909	0.952	0.997	0.932	0.964
2	0.936	0.807	0.867	0.920	0.837	0.876	0.935	0.886	0.910
3	0.696	0.944	0.801	0.787	0.801	0.794	0.798	0.900	0.846
4	0.811	0.991	0.892	0.883	0.954	0.917	0.906	0.988	0.945
5	0.492	0.897	0.636	0.514	0.854	0.642	0.534	0.885	0.667
6	0.674	0.836	0.746	0.634	0.964	0.765	0.858	0.875	0.866
	Average F1: 0.814 Accuracy: 0.872 Average F1*: 0.736 Accuracy*: 0.723			Average F1: 0.824 Accuracy: 0.886 Average F1*: 0.742 Accuracy*: 0.730			Average F1: 0.866 Accuracy: 0.920 Average F1*: 0.800 Accuracy*: 0.845		

*20 times more weight on facies 3, 5, and 6 than facies 1, 2, and 4, considering their greater geologic implication and interpretational importance.

2D along validation section IL150 (Figures 12d–12g). Table 1 lists the corresponding statistics including precision, recall, F1, and accuracy of the predicted facies from all four iterations by comparing it to the expert annotation of the entire cube, excluding the training sections. This clearly demonstrates the improvement of facies identification through the iterative process. In this example, based on the provided volumetric manual annotation, the criteria of terminating the iterative process are defined as the accuracy and average F1 reaching 0.95 and 0.9, respectively. By lifting the threshold, the process can continue with more iterations and lead to better accuracy. However, this requires more computational resources.

Next, to validate the added values of the proposed RRE-based recommendation, we compare it to two training-data-selection strategies: one is the manual screening, and the other is the clustering-based recommendation (Manikani et al., 2022). In this experiment, nine sections are selected by each strategy and used for training the same DT-CNN. Figure 10 shows their spatial layout within the Parihaka survey. The corresponding facies

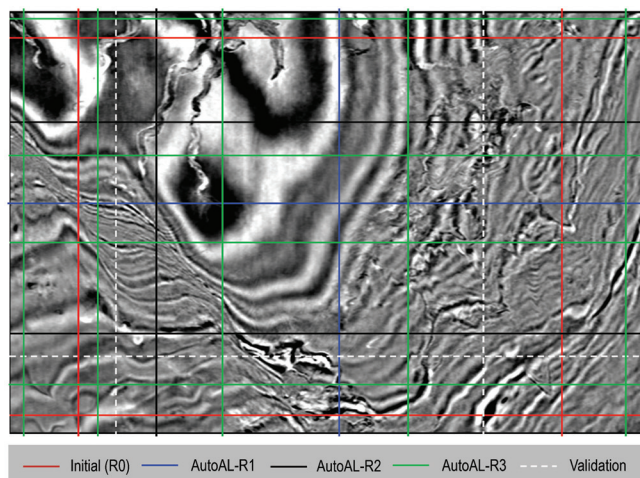


Figure 7. The layout of the 2D sections involved while applying the proposed iterative workflow including the four initial sections (red), two sections recommended after iteration 1 (blue), three sections recommended after iteration 2 (black), nine sections recommended after iteration 3 (green), and three validation sections (dotted white).

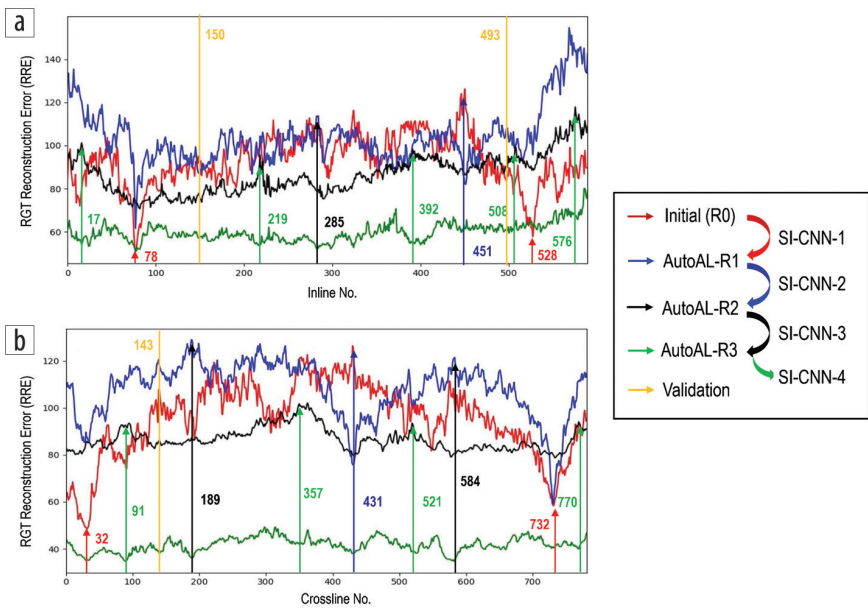


Figure 8. The RGT RRE along (a) inline and (b) crossline directions as well as the corresponding training section recommendation after each iteration while applying the proposed iterative workflow.

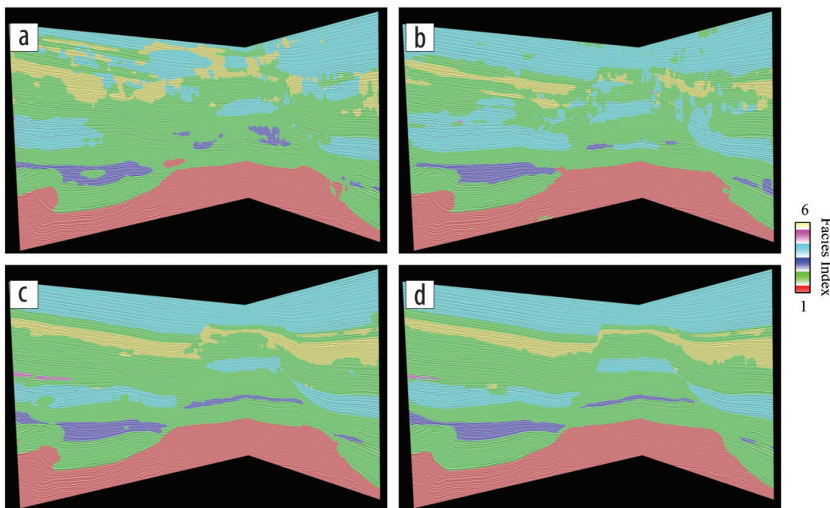
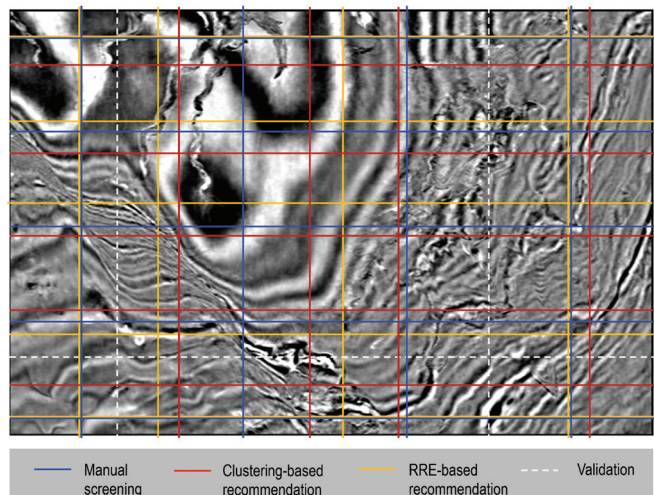


Figure 9. A 3D view of facies predictions along validation sections IL493 and XL143 while applying the proposed workflow in four iterations (a-d). The prediction accuracy is significantly improved from iteration 1 to 4.

Figure 10. The layout of three sets of training sections used for comparing their impact on training the same DT-CNN, with the manual screening set in blue, the clustering-based recommendation in red, and the RRE-based recommendation in orange. Each set is of nine sections. The dotted white lines represent the three validation sections in the experiment, which are the same as those in Figure 7.



prediction is visually shown in 3D along validation sections IL493 and XL143 (Figure 11) and 2D along validation section IL150 (Figures 12f, 12h, and 12i). It is also quantitatively evaluated by the statistics (Table 2), in which the RRE-based recommendation leads to best scores on all six facies, especially the three small facies (3, 5, and 6).

Conclusions

This work proposes enabling interactive machine learning-based seismic image interpretation by integrating AL with automated training data recommendation through a DT-CNN: one for seismic interpretation and the other for RGT reconstruction. By such coupling, the curve of RRE, with respect to the section, is observed and indicative of how accurate the CNN prediction is per section. Thus, it can be used for fast screening and recommending most representative sections for learning in the next iteration. Its added value is well demonstrated in the use case of facies classification on the Parihaka seismic survey, with the machine accuracy reaching 0.9 after four iterations. In addition to the RGT used in this paper, other seismic properties such as the velocity model can fit the proposed AutoAL workflow. **TLE**

Acknowledgments

We would like to thank the assistant editor Madhumita Sengupta and associate editor Vladimir Kazei. We thank the reviewers, Anton Egorov and

one anonymous expert, for their helpful insights and suggestions, which helped improve the quality and clarity of the paper. We also thank New Zealand Crown Minerals and Chevron for providing the Parihaka seismic data set and the manual six-facies annotation, respectively. The nine manually selected clustering-recommended training sections used for comparisons were provided by Leigh Truelove and Sunil Manikani at Schlumberger.

The neural networks were developed using the open-source software library TensorFlow, which was developed by the Google Brain Team.

Data and materials availability

Data associated with this research are available and can be obtained by contacting the corresponding author.

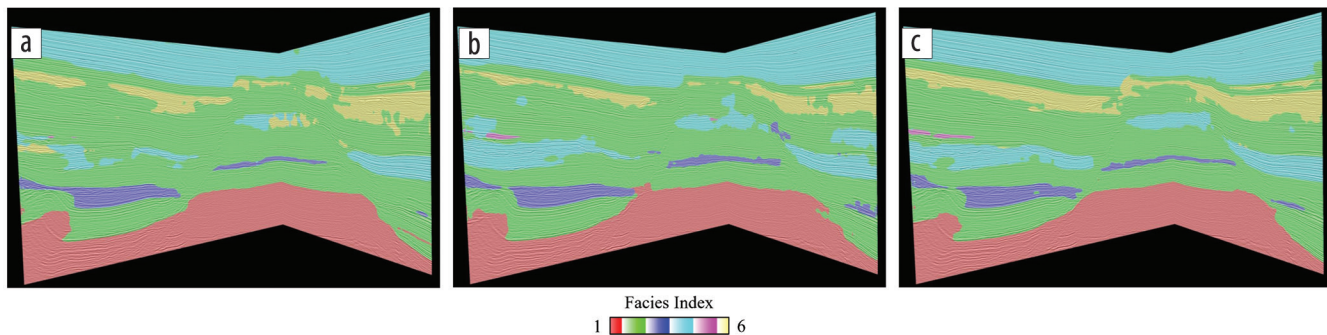


Figure 11. A 3D view of facies predictions along validation sections IL493 and XL143 by training the same DT-CNN using three different sets of training sections as illustrated in Figure 10. The RRE-based recommendation leads to best prediction accuracy and minimal artifacts.

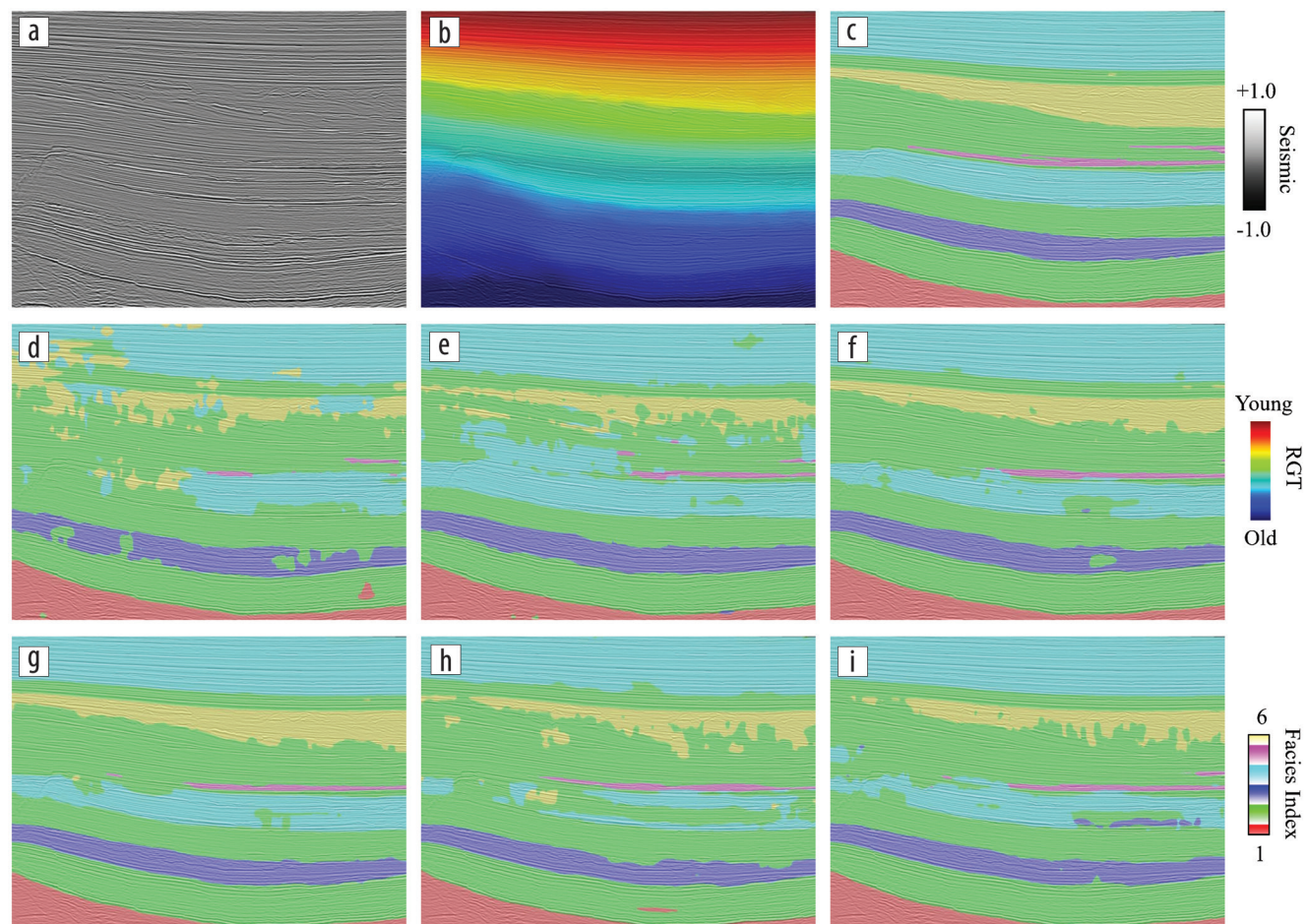


Figure 12. A 2D view along validation section IL150 including (a) seismic amplitude, (b) RGT, (c) manual annotation and facies predictions from (d) the four initial training sections (R0), (e) the six training sections recommended after AutoAL-R1, (f) the nine training sections recommended after AutoAL-R2, (g) the 18 training sections recommended after AutoAL-R3, (h) the nine training sections selected after manual screening, and (i) the nine sections recommended after the clustering algorithm. Note, the increasing accuracy from iteration 1 to 4 (d–g) as well as the improved quality by using the RRE-based scheme over the manual screening and clustering-based scheme for training data selection.

References

- Bahorich, M., and S. Farmer, 1995, 3-D seismic discontinuity for faults and stratigraphic features: The coherence cube: *The Leading Edge*, **14**, no. 10, 1053–1058, <https://doi.org/10.1190/1.1437077>.
- Barnes, A. E., 2007, A tutorial on complex seismic trace analysis: *Geophysics*, **72**, no. 6, W33–W43, <https://doi.org/10.1190/1.2785048>.
- Das, S., W.-K. Wong, T. Dietterich, A. Fern, and A. Emmott, 2016, Incorporating expert feedback into active anomaly discovery: 16th International Conference on Data Mining, IEEE, Extended Abstracts, <https://doi.org/10.1109/ICDM.2016.0102>.
- Di, H., and G. AlRegib, 2020, A comparison of seismic saltbody interpretation via neural networks at sample and pattern levels: *Geophysical Prospecting*, **68**, no. 2, 521–535.
- Di, H., and D. Gao, 2017, 3D seismic flexure analysis for subsurface fault detection and fracture characterization: *Pure and Applied Geophysics*, **174**, 747–761, <https://doi.org/10.1007/s0024-016-1406-9>.
- Di, H., M. A. Shafiq, and G. AlRegib, 2018a, Multi-attribute k -means clustering for salt-boundary delineation from three-dimensional seismic data: *Geophysical Journal International*, **215**, no. 3, 1999–2007, <https://doi.org/10.1093/gji/ggy376>.
- Di, H., Z. Wang, and G. AlRegib, 2018b, Seismic fault detection from post-stack amplitude by convolutional neural networks: 80th Conference and Exhibition, EAGE, Extended Abstracts, <https://doi.org/10.3997/2214-4609.201800733>.
- Di, H., M. A. Shafiq, Z. Wang, and G. AlRegib, 2019, Improving seismic fault detection by super-attribute-based classification: *Interpretation*, **7**, no. 3, SE251–SE267, <https://doi.org/10.1190/INT-2018-0188.1>.
- Di, H., Z. Li, H. Maniar, and A. Abubakar, 2020, Seismic stratigraphy interpretation by deep convolutional neural networks: A semisupervised workflow: *Geophysics*, **85**, no. 4, WA77–WA86, <https://doi.org/10.1190/geo2019-0433.1>.
- Di, H., Z. Li, and A. Abubakar, 2022, Using relative geologic time to constrain convolutional neural network-based seismic interpretation and property estimation: *Geophysics*, **87**, no. 2, IM25–IM35, <https://doi.org/10.1190/geo2021-0257.1>.
- Gao, D., 2003, Volume texture extraction for 3D seismic visualization and interpretation: *Geophysics*, **68**, no. 4, 1294–1302, <https://doi.org/10.1190/1.1598122>.
- Guitton, A., 2018, 3D convolutional neural networks for fault interpretation: 80th Conference and Exhibition, EAGE, Extended Abstracts, <https://doi.org/10.3997/2214-4609.201800732>.
- Guo, Y., S. Peng, W. Du, and D. Li, 2020, Fault and horizon automatic interpretation by CNN: A case study of coalfield: *Journal of Geophysics and Engineering*, **17**, no. 6, 1016–1025, <https://doi.org/10.1093/jge/gxa060>.
- Hale, D., 2013, Methods to compute fault images, extract fault surfaces, and estimate fault throws from 3D seismic images: *Geophysics*, **78**, no. 2, O33–O43, <https://doi.org/10.1190/geo2012-0331.1>.
- Huang, L., X. Dong, and T. E. Clee, 2017, A scalable deep learning platform for identifying geologic features from seismic attributes: *The Leading Edge*, **36**, no. 3, 249–256, <https://doi.org/10.1190/tle36030249.1>.
- Li, Z., and A. Abubakar, 2020, Complete sequence stratigraphy from seismic optical flow without human labeling: 90th Annual International Meeting, SEG, Expanded Abstracts, 1248–1252, <https://doi.org/10.1190/segam2020-3427292.1>.
- Li, Z., H. Di, H. Maniar, and A. Abubakar, 2019, Semi-supervised deep machine learning assisted seismic image segmentation and stratigraphic sequence interpretation: 81st Conference and Exhibition, EAGE, Extended Abstracts, <https://doi.org/10.3997/2214-4609.201901389>.
- Manikani, S., H. Di, L. Truelove, and C. Li, 2022, Quantifying diversity in seismic datasets: U.S. patent 63/362,777.
- Marfurt, K. J., and R. L. Kirlin, 2000, 3-D broad-band estimates of reflector dip and amplitude: *Geophysics*, **65**, no. 1, 304–320, <https://doi.org/10.1190/1.1444721>.
- Marfurt, K. J., R. L. Kirlin, S. L. Farmer, and M. S. Bahorich, 1998, 3-D seismic attributes using a semblance-based coherency algorithm: *Geophysics*, **63**, no. 4, 1150–1165, <https://doi.org/10.1190/1.1444415>.
- Peters, B., J. Granek, and E. Haber, 2019, Multi-resolution neural networks for tracking seismic horizons from few training images: *Interpretation*, **7**, no. 3, SE201–SE213, <https://doi.org/10.1190/INT-2018-0225.1>.
- Roberts, A., 2001, Curvature attributes and their application to 3D interpreted horizons: *First Break*, **19**, no. 2, 85–100, <https://doi.org/10.1046/j.0263-5046.2001.00142.x>.
- Robertson, J. D., and D. A. Fisher, 1988, Complex seismic trace attributes: *Geophysics*, **7**, no. 6, 22–26, <https://doi.org/10.1190/1.1439517>.
- Roy, A., M. Matos, and K. J. Marfurt, 2010, Automatic seismic facies classification with Kohonen self-organizing maps — A tutorial: *Geohorizons*, 6–14.
- Shi, Y., X. Wu, and S. Fomel, 2019, SaltSeg: Automatic 3D salt segmentation using a deep convolutional neural network: *Interpretation*, **7**, no. 3, SE113–SE122, <https://doi.org/10.1190/INT-2018-0235.1>.
- Taner, M. T., F. Koehler, and R. E. Sheriff, 1979, Complex seismic trace analysis: *Geophysics*, **44**, no. 6, 1041–1063, <https://doi.org/10.1190/1.1440994>.
- Tingdahl, K. M., and M. de Rooij, 2005, Semi-automatic detection of faults in 3D seismic data: *Geophysical Prospecting*, **53**, no. 4, 533–542, <https://doi.org/10.1111/j.1365-2478.2005.00489.x>.
- Tschannen, V., M. Delescluse, N. Ettrich, and J. Keuper, 2020, Extracting horizon surfaces from 3D seismic data using deep learning: *Geophysics*, **85**, no. 3, N17–N26, <https://doi.org/10.1190/geo2019-0569.1>.
- Waldehand, A. U., A. C. Jensen, L.-J. Gelius, and A. H. S. Solberg, 2018, Convolutional neural networks for automated seismic interpretation: *The Leading Edge*, **37**, no. 7, 529–537, <https://doi.org/10.1190/tle37070529.1>.
- Wu, X., 2016, Methods to compute salt likelihoods and extract salt boundaries from 3D seismic images: *Geophysics*, **81**, no. 6, IM119–IM126, <https://doi.org/10.1190/geo2016-0250.1>.
- Wu, X., L. Liang, Y. Shi, and S. Fomel, 2019a, FaultSeg3D: Using synthetic data sets to train an end-to-end convolutional neural network for 3D seismic fault segmentation: *Geophysics*, **84**, no. 3, IM35–IM45, <https://doi.org/10.1190/geo2018-0646.1>.
- Wu, H., B. Zhang, T. Lin, D. Cao, and Y. Lou, 2019b, Semiautomated seismic horizon interpretation using the encoder-decoder convolutional neural network: *Geophysics*, **84**, no. 6, B403–B417, <https://doi.org/10.1190/geo2018-0672.1>.
- Xiong, W., X. Ji, Y. Ma, Y. Wang, N. M. AlBinHassan, M. N. Ali, and Y. Luo, 2018, Seismic fault detection with convolutional neural network: *Geophysics*, **83**, no. 5, O97–O103, <https://doi.org/10.1190/geo2017-0666.1>.
- Zheng, Z., P. Kavousi, and H. Di, 2014, Multi-attributes and neural network-based fault detection in 3D seismic interpretation: *Advanced Materials Research*, 1497–1502.